



Article

Purifying High-Purity Copper via Semi-Continuous Directional Solidification: Insights from Numerical Simulations

Yao Wu ^{1,2}, Yunhu Zhang ^{1,2}, Long Zeng ³ and Hongxing Zheng ^{1,2,*}

¹ School of Materials Science and Engineering, Shanghai University, Shanghai 200444, China; wuyao21722464@163.com (Y.W.); zhangyunh.zyh@163.com (Y.Z.)

² Shanghai Engineering Research Center for Integrated Circuits and Advanced Display Materials, Shanghai University, Shanghai 200444, China

³ School of Materials Science and Engineering, Shanghai Jiao Tong University, Shanghai 200240, China; recrystal@sjtu.edu.cn

* Correspondence: hxzheng@shu.edu.cn

Abstract: High-purity copper is essential for fabricating advanced microelectronic devices, particularly integrated circuit interconnects. As the industry increasingly emphasizes scalable and efficient purification methods, this study investigates the multi-physics interactions during the semi-continuous directional solidification process, utilizing a Cu-1 wt.%Ag model alloy. Coupled simulation calculations examine the spatial distribution patterns of the impurity element silver (Ag) within semi-continuously solidified ingots under varying pulling rates and melt temperatures. The objective is to provide technical insights into the utilization of the semi-continuous directional solidification method for high-purity copper purification. The findings reveal that increasing the pulling rate and melt temperature leads to a downward shift in the solid–liquid interface relative to the mold top during processing. Alongside the primary clockwise vortex flow, a secondary weak vortex emerges near the solid–liquid interface, facilitating the migration of the impurity element Ag toward the central axis and amplifying radial impurity fluctuations. Furthermore, diverse pulling rates and melt temperature conditions unveil a consistent trend along the ingot’s height, which is characterized by an initial increase in average Ag content, followed by stabilization and then a rapid ascent during the late stage of solidification, with higher pulling rates and melt temperatures expediting this rapid ascent. Leveraging these insights, a validation experiment using 4N-grade recycled copper in a small-scale setup demonstrates the effectiveness of the semi-continuous directional solidification process for high-purity copper production, with copper samples extracted at 1/4 and 3/4 ingot heights achieving a 5N purity level of 99.9994 wt.% and 99.9993 wt.%, respectively.

Keywords: high-purity copper; numerical simulation; solid–liquid interface; semi-continuous directional solidification



Citation: Wu, Y.; Zhang, Y.; Zeng, L.; Zheng, H. Purifying High-Purity Copper via Semi-Continuous Directional Solidification: Insights from Numerical Simulations. *Separations* **2024**, *11*, 176. <https://doi.org/10.3390/separations11060176>

Academic Editors:
Victoria Samanidou and
George Zachariadis

Received: 7 May 2024

Revised: 28 May 2024

Accepted: 1 June 2024

Published: 5 June 2024



Copyright: © 2024 by the authors. Licensee MDPI, Basel, Switzerland. This article is an open access article distributed under the terms and conditions of the Creative Commons Attribution (CC BY) license (<https://creativecommons.org/licenses/by/4.0/>).

1. Introduction

High-purity copper possesses exceptional thermal and electrical conductivity, rendering it an essential material for manufacturing microelectronic components such as integrated circuit interconnects, printed circuit boards, and connectors. This property is particularly crucial for very-large-scale integrated circuits, where minimizing signal transmission delays is imperative [1,2]. Concurrently, the ever-shortening lifespan of electronic products has led to a staggering increase in waste electrical and electronic equipment (WEEE), exerting tremendous pressure on copper recovery [3]. Various methods exist for producing high-purity copper, including electrolytic refining, vacuum distillation, electron-beam refining, zone refining, and directional solidification, each with distinct advantages and limitations. Selecting the most suitable approach necessitates a comprehensive evaluation of factors such as the initial raw material purity, types of impurities, target purity levels, and equipment investment.

Electrolytic refining involves the electrochemical separation of impurities from low-purity copper. Although relatively straightforward and suitable for large-scale production, this process consumes significant amounts of energy and raises environmental concerns. Optimization efforts have focused on adjusting parameters like the current density, electrolyte temperature, and composition to enhance production and energy efficiency [4–6]. Notably, Ding et al. explored using a non-dissolving lead dioxide electrode coupled with copper oxide addition to improve cathode copper quality and current efficiency, potentially leading to energy savings and reduced material consumption [7]. Wang et al. proposed an efficient system for high-purity copper recycling from waste printed circuit boards using an ammonia–ammonium carbonate slurry electrolysis process, achieving a 90.4% recovery rate and 99.97 wt.% pure copper under optimal conditions [8].

Vacuum distillation exploits the differential sublimation temperatures and condensation characteristics of copper and impurities for purification [9–12]. For instance, Wang et al. determined separation coefficients, plotted vapor–liquid equilibrium phase diagrams, and discussed the effects of temperature, holding time, and system pressure, achieving up to 99.9993 wt.% purity at 1473 K, 1.5 h, and 5 Pa [9]. Electron-beam refining involves focusing high-energy electron beams to bombard metal, thereby purifying it through processes like degassing, decomposition, deoxidation, and impurity evaporation or floating [13–15]. Zone refining relies on the differential solubility of impurities in the solid and liquid phases to facilitate their migration from locally molten zones and to achieve purification. In addition to traditional studies exploring how process parameters like multi-pass operation, melting temperature, molten zone width, and moving rate influence the impurity separation efficiency [16–18], Zhu et al. investigated the effects of floating-zone refining at reduced hydrogen pressure on copper purification, finding that nearly all impurities could be significantly reduced with removal mechanisms involving reactions with hydrogen and the convective transport of inclusions [19]. Unlike electrolytic refining, these three methods offer the advantage of attaining higher-purity copper by effectively eliminating various impurities, including oxygen, sulfur, and carbon, without generating wastewater or gaseous emissions. However, they collectively face challenges such as high levels of equipment investment and elevated energy consumption.

Additionally, directional solidification involves applying controllable heat flow to induce specific crystal growth, like in zone refining, to physically segregate impurities. Fu et al. achieved a significant reduction in impurities by producing 5N high-purity copper through vacuum distillation and directional solidification. They found that the segregation effect can be remarkable when the equilibrium partition coefficient (k_0) value is less than 0.65, attributed to copper's strong affinity for certain metallic and non-metallic impurities [20]. Similarly, Huang et al. utilized electron-beam refining and directional solidification to eliminate metallic impurities from metallurgical-grade silicon for solar applications, with removal ratios exceeding 95% in the ingot's bottom part [21]. Notably, from a scaled-up production perspective, the semi-continuous directional solidification method, also known as semi-continuous casting, has already been applied to the preparation of high-purity aluminum [22], thus sparking interest in scaling up high-purity copper production using this method.

This study employs numerical simulation methods to examine the multi-physics fields during the semi-continuous directional solidification process of high-purity copper. Silver (Ag) serves as a representative impurity element in the simulations. The focus is on investigating the effects of two key process parameters: copper melt temperature and ingot pulling rate. Specifically, the study aims to understand their impact on the solid–liquid interface, melt flow at the interface front, and the separation efficiency of impurities. The objective is to provide a theoretical basis and technical support for optimizing parameters in the semi-continuous directional solidification process, which will facilitate the scaled-up production of high-purity copper.

2. Numerical Simulation Method

2.1. Numerical Simulation Physical Model

This study employs the ANSYS Fluent software (Fluent 2022 R1) and a continuum modeling approach to simulate the semi-continuous directional solidification process of a Cu-1 wt.%Ag alloy. The simulation couples models for fluid flow, heat transfer, solidification, and solute transport [23,24]. The enthalpy–porosity technique [25] is utilized to represent the solidification process, while the solute transport is governed by the Lever Rule. The following assumptions form the mathematical foundation:

1. Thermal–solutal convection is described by the Boussinesq approximation, which considers density variations only in the buoyancy term while treating the remaining densities as constants.
2. The melt flow during the semi-continuous directional solidification process is assumed to be laminar and incompressible.
3. The solidification process is governed by the condition of local thermodynamic equilibrium.
4. Physical properties, except for density, are considered invariant with respect to temperature.
5. The solid phase is assumed to be non-deformable and free from internal stresses.
6. The sum of the volume fractions of the solid and liquid phases in the mushy zone is unity.

The governing equations employed in this study are as follows:

Continuity equation:

$$\frac{\partial \rho}{\partial t} + \nabla \cdot (\rho \vec{v}) = 0 \quad (1)$$

where ρ denotes density, t represents time, and \vec{v} stands for the velocity vector.

Momentum equation:

$$\frac{\partial}{\partial t} (\rho \vec{v}) + \nabla \cdot (\rho \vec{v} \vec{v}) = -\nabla p + \nabla \cdot (\mu \nabla \vec{v}) + \rho \vec{g} + \vec{S} + \vec{F} \quad (2)$$

$$\vec{S} = \frac{f_s^2}{f_s^3 + \varepsilon} A_{mush} (\vec{v} - \vec{v}_s) \quad (3)$$

$$\vec{F} = -\rho \vec{g} [\beta_T (T - T_{ref}) + \beta_C (C_l - C_{ref})] \quad (4)$$

$$T_{ref} = \frac{T_0 + T_s}{2} \quad (5)$$

$$C_{ref} = \frac{C_0 + C_{end}}{2} \quad (6)$$

where p represents the pressure; μ represents the dynamic viscosity; \vec{g} denotes the gravitational acceleration; \vec{S} represents the momentum source term; \vec{F} represents the thermal and solute buoyancy; f_s represents the solid-phase fraction; ε represents a small value to prevent meaningless fractions, set as $\varepsilon = 0.001$ in this study; A_{mush} represents the mushy zone constant, with a value of 10^8 ; \vec{v}_s represents the velocity of the solid phase; T represents the melt temperature; T_{ref} represents the reference temperature; T_s represents the solidus temperature; T_0 represents the initial temperature; β_T represents the thermal expansion coefficient; β_C represents the solute expansion coefficient; C_{ref} represents the reference content of the solute; C_l represents the content of the solute in the liquid phase; C_0 represents the initial content of the solute; and C_{end} represents the solidified end content of the solute.

Energy conservation:

$$\frac{\partial}{\partial t} (\rho H) + \nabla \cdot (\rho \vec{v} H) = \nabla \cdot (K \nabla T) \quad (7)$$

$$H = h + \Delta H \tag{8}$$

$$h = h_{ref} + \int_{T_{ref}}^T C_p dT \tag{9}$$

$$\Delta H = f_l \Delta H_f \tag{10}$$

$$f_l = \begin{cases} 0 & T < T_s \\ \frac{T-T_s}{T_l-T_s} & T_s \leq T \leq T_l \\ 1 & T > T_l \end{cases} \tag{11}$$

where H represents enthalpy, K denotes thermal conductivity, h represents sensible enthalpy, ΔH represents latent heat, h_{ref} represents the reference of enthalpy, C_p represents the specific heat capacity, ΔH_f represents the latent heat of fusion, T_l represents the liquidus temperature, and f_l represents the liquid-phase fraction.

Solute conservation:

$$\frac{\partial}{\partial t}(\rho C) + \nabla \cdot (\rho \vec{v} C) = \nabla \cdot (\rho D \nabla C) + \nabla \cdot [\rho D \nabla (C_l - C)] - \nabla \cdot [\rho (C_l - C) \vec{v}] \tag{12}$$

where C represents the solute content, and D represents the solute diffusion coefficient. In the Lever segregation model, it is assumed that the solid–liquid interface has reached local thermodynamic equilibrium, and the partition of solutes follows:

$$C_l = C[1 - (1 - k_0) \cdot f_s]^{-1} \tag{13}$$

$$C_s = k_0 C[1 - (1 - k_0) \cdot f_s]^{-1} \tag{14}$$

where k_0 represents the solute equilibrium partition coefficient, and C_s represents the content of the solute in the solid phase.

2.2. Geometric Model and Boundary Conditions

Figure 1 illustrates the appearance of the semi-continuous directional solidification apparatus and a schematic representation of its internal structure. The experimental procedure is as follows: Initially, recycled copper raw material is introduced into a graphite crucible with a diameter of 250 mm. Subsequently, the furnace is evacuated and maintained at a vacuum level of ≤ 5 Pa throughout the operation, employing medium-frequency induction heating. The temperature of the copper melt is monitored and controlled using a thermocouple positioned on the outer wall of the graphite crucible. Upon reaching the preset heating temperature, the melt is held for a specific duration. Following this, the downward pulling system is activated, allowing the melt within the crucible to flow into a graphite mold with a diameter of 160 mm through a 100 mm diameter orifice. The pulling rate remains constant, facilitating the directional solidification of high-purity copper and promoting the impurity separation.

Considering the cylindrical ingot shape, this study simplifies the system into a two-dimensional axisymmetric model for numerical simulation. In the apparatus, the graphite crucible inductively heats the copper melt, serving as the heating element. Previous studies [26,27] validate the crucible’s effective electromagnetic shielding during induction heating. Therefore, this study disregards melt flow inside the graphite crucible, focusing solely on simulating the directional solidification process of the melt below the crucible bottom. The initial melt velocity V_{inlet} at the mold inlet is derived from mass flow conservation (Equation (15)):

$$V_{inlet} = V_{pull} \times \frac{R_{outlet}^2}{R_{inlet}^2} \tag{15}$$

where R_{outlet} represents the radius at the mold outlet, R_{inlet} represents the radius at the melt inlet, and V_{pull} represents the pulling rate of the semi-continuous directional solidification process.

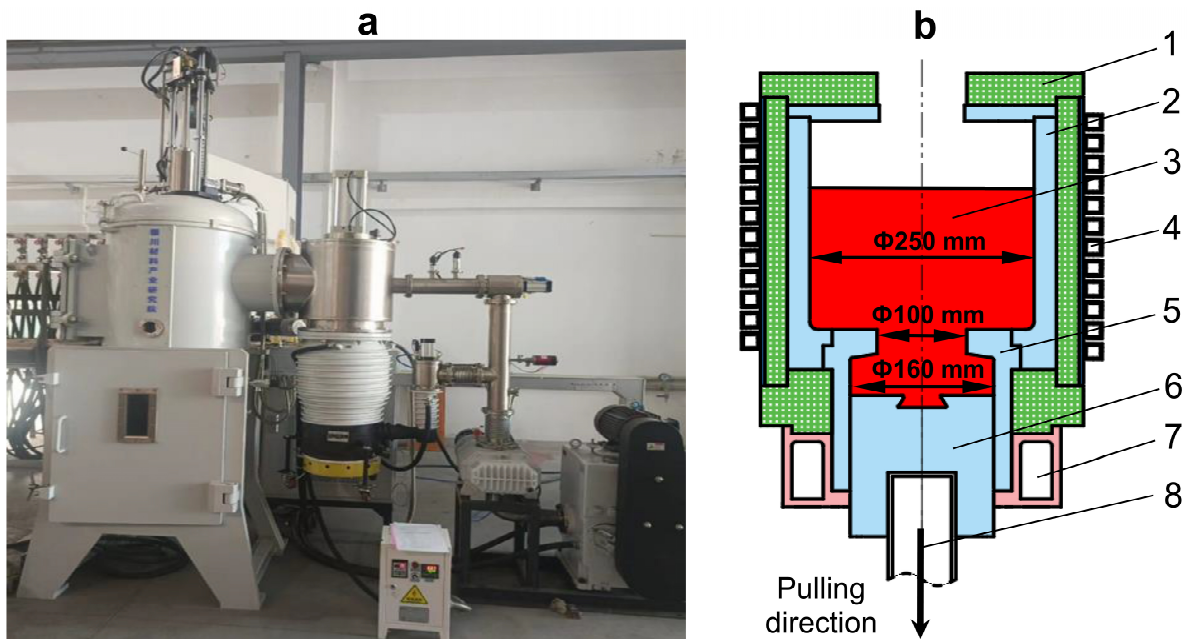


Figure 1. (a) Apparatus for the semi-continuous directional solidification process. (b) Internal structure. Key components: 1. Hard-graphite-felt insulation layer; 2. Graphite crucible; 3. Copper melt; 4. Water-cooled copper induction heating coil; 5. Graphite sleeve; 6. Graphite traction disk; 7. Water-cooled copper tube; 8. Water-cooled stainless steel pulling rod.

Figure 2 depicts the ingot model geometry (160 mm diameter) and boundary conditions, where the 100 mm diameter melt inlet is the velocity inlet, and all other boundaries employ no-slip conditions with zero solute flux. The initial computation height is 15 mm, with a final ingot height of 415 mm. The model is partitioned into square grids with a 2 mm side length. Following the literature [28], the side walls of the ingot are divided into 5 distinct thermal exchange zones with the surroundings:

Zone 1 (height 20 mm): The graphite sleeve contact has a heat transfer coefficient of 0.

Zone 2 (height 80 mm): The graphite sleeve and insulation layer contact area features an effective heat transfer coefficient of $100 \text{ W}/(\text{m}^2 \cdot \text{K})$.

Zone 3 (height 70 mm): The graphite sleeve and water-cooled copper tube interface assumes a heat transfer coefficient of $200 \text{ W}/(\text{m}^2 \cdot \text{K})$.

Zone 4 (height 20 mm): The direct contact between ingot and water-cooled copper tube provides substantial cooling with a heat transfer coefficient of $500 \text{ W}/(\text{m}^2 \cdot \text{K})$.

Zone 5: Primarily dissipating heat through radiation, this region simplifies to a heat transfer coefficient of $30 \text{ W}/(\text{m}^2 \cdot \text{K})$.

Additionally, at the bottom of the ingot, the heat transfer coefficient is set to $500 \text{ W}/(\text{m}^2 \cdot \text{K})$. The relevant physical properties of the Cu-1 wt.%Ag alloy used in the calculation are presented in Table 1 [20,29,30].

This study adopts a control variable approach to simulate the transient distribution characteristics of the impurity element Ag along the height direction of the copper ingot under two melt temperature conditions: 1400 K and 1420 K, with pulling rates of $25 \mu\text{m}/\text{s}$, $50 \mu\text{m}/\text{s}$, and $100 \mu\text{m}/\text{s}$. User-defined functions (UDFs) facilitate the downward pulling during directional solidification by incorporating dynamic mesh capabilities and variable heat transfer coefficients into the coupled computation of temperature, solute, and flow fields. The SIMPLE algorithm is employed to solve the governing equations. A time step of 0.01 s is adopted, with a maximum of 40 iterations per time step. The momentum equations are discretized using a second-order upwind scheme, while the other equations are discretized using a first-order upwind scheme. The solution is considered converged when the residuals for the continuity, momentum, and solute equations are less than 10^{-3} , and the residual for the energy equation is less than 10^{-6} .

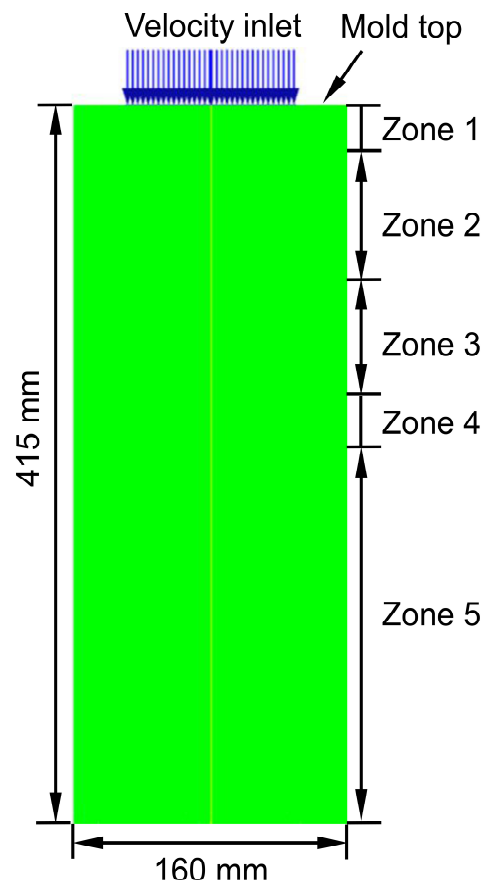


Figure 2. Geometric model dimensions and boundary conditions for thermal exchange used in the numerical simulations.

Table 1. Physical properties of the Cu-1 wt.% Ag alloy used in the simulations.

Parameter	Value	Parameter	Value
Density at 293.15 K, ρ (kg·m ⁻³)	8920	Liquid temperature, T_l (K)	1348
Thermal conductivity, K (W·(m·K) ⁻¹)	401	Slope of the liquidus, m (K·(wt.%) ⁻¹)	-5.04
Latent heat, ΔH_f (J·kg ⁻¹)	2.05×10^5	Thermal expansion coefficient, β_T (K ⁻¹)	1.66×10^{-5}
Specific heat, C_p (J·(kg·K) ⁻¹)	385	Solute expansion coefficient, β_C (wt.%) ⁻¹)	3.2×10^{-3}
Dynamic viscosity, μ (kg·(m·s) ⁻¹)	3.20×10^{-3}	Diffusion coefficient, D (m ² ·s ⁻¹)	3.6×10^{-9}
Solid temperature, T_s (K)	1351	Equilibrium partition coefficient, k_0	0.65

3. Results and Discussion

3.1. Migration and Distribution of the Impurity Element Ag during the Semi-Continuous Directional Solidification Process

This section explores the migration behavior governing the spatial distribution of the impurity element Ag during the semi-continuous directional solidification process. The experimental conditions involve a melt temperature of 1400 K and a pulling rate of 50 $\mu\text{m/s}$. Numerical simulations unveil the spatial distribution map of Ag within the ingot at distinct time points during solidification, as depicted in Figure 3. Notably, Ag exhibits pronounced enrichment in the central region of the solid–liquid interface. The enrichment pattern along the ingot’s height undergoes a complex evolution, characterized by a gradual ascent, subsequent descent, and eventual sharp escalation. Additionally, a progressive reduction in the distance is observed between the solid–liquid interface and the mold top, facilitating the flattening of the interface and increased the Ag content in the liquid phase above.

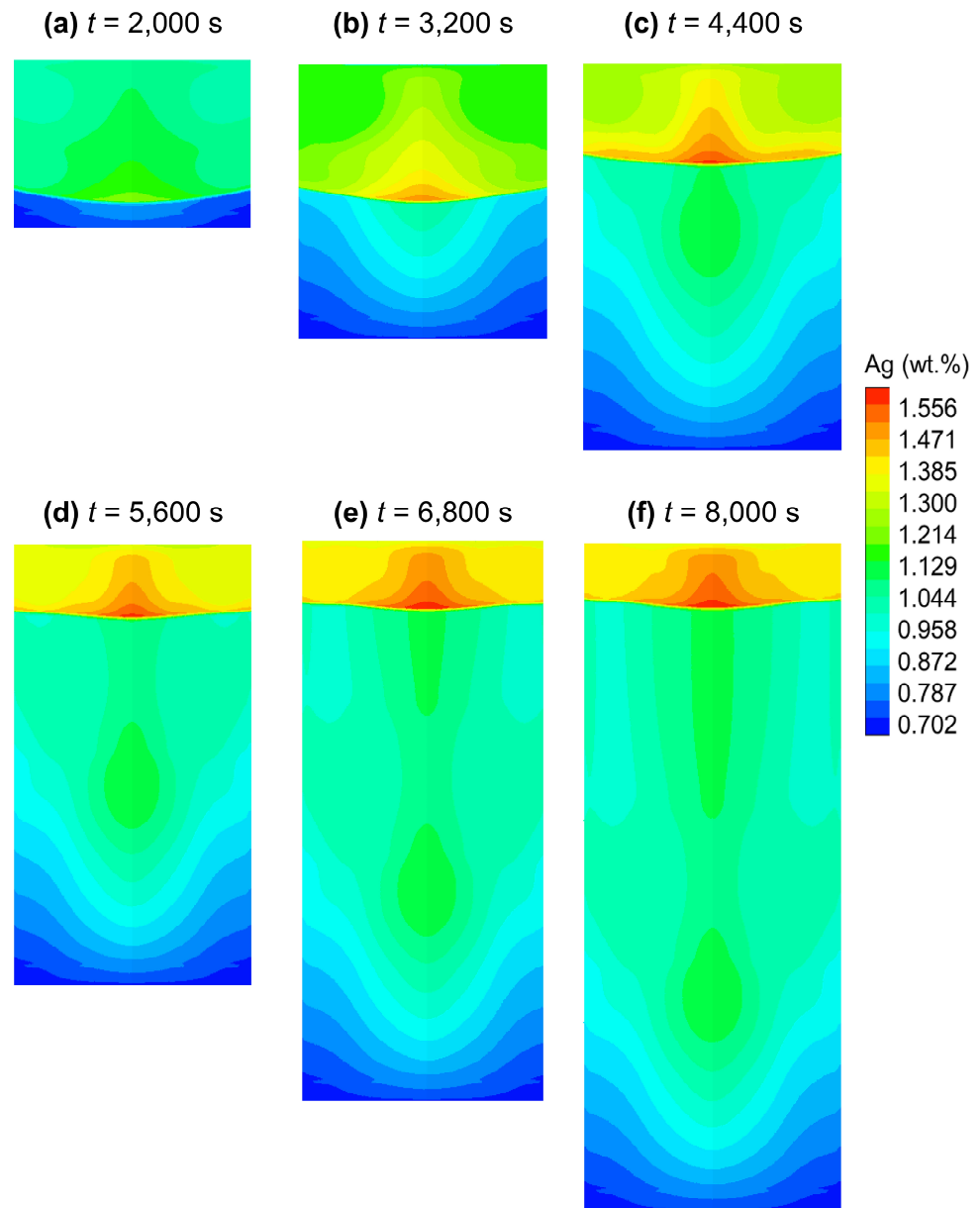


Figure 3. Simulated spatial and temporal evolution of distribution of the impurity element Ag throughout the semi-continuous directional solidification process. Conditions: melt temperature of 1400 K and a pulling rate of 50 $\mu\text{m/s}$.

Figure 4 elucidates the distribution profiles of the impurity element Ag along both the axial centerline and the radial direction of the ingot at various time points. Initially, as depicted in Figure 4a, the Ag content along the axial centerline exhibits a continuous rise when the solidification height (h) of the copper ingot is below 135 mm. Within the solidification height range of 135 mm to 205 mm, a gradual decline in Ag content is observed, followed by stabilization at 1.10 wt.% at a height of 244 mm before a notable surge at the height of 373 mm. Furthermore, significant fluctuations in the radial Ag content are observed in Figure 4b, with maximum–minimum differences of 0.17 wt.%, 0.16 wt.%, 0.07 wt.%, 0.11 wt.%, 0.20 wt.%, and 0.39 wt.% at ingot heights of 80 mm, 155 mm, 230 mm, 305 mm, 380 mm, and 415 mm, respectively.

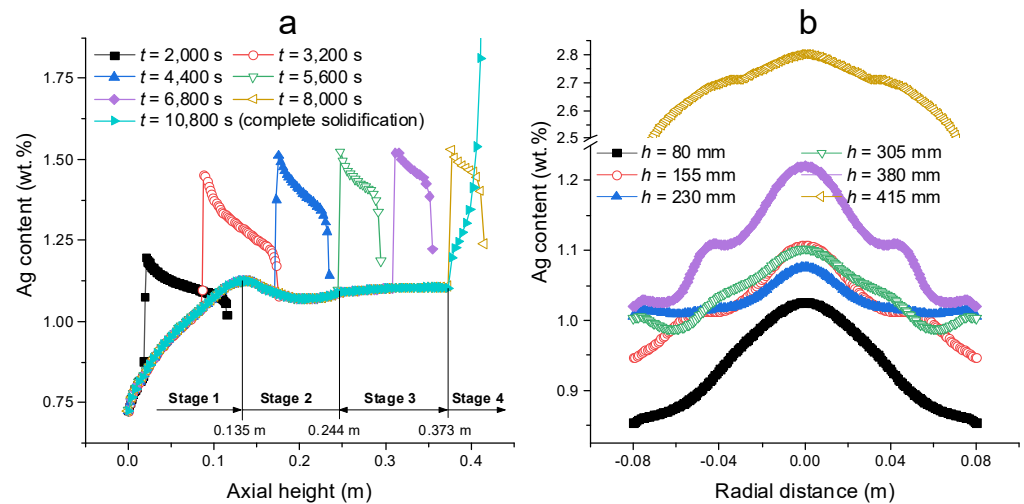


Figure 4. (a) Simulated axial distribution of the impurity element Ag along the central axis of the copper ingot at different time points. (b) Simulated radial distribution of Ag across various heights of the ingot during the solidification process. Conditions: melt temperature of 1400 K and a pulling rate of 50 $\mu\text{m/s}$.

Melt flow, driven by temperature-induced density differences, emerges as the primary factor influencing the spatial impurity distribution in the present study, which is markedly different from electromagnetic semi-continuous directional solidification [31]. To deepen the understanding of Ag distribution patterns, Figure 5 presents the evolution of temperature and flow fields alongside the solid–liquid interface at corresponding time points. The evolving temperature field maps on the left side of Figure 5 reveal that at the initial stage, a sparse distribution of isotherms characterizes the forefront of the solid–liquid interface (lower thermal gradient) owing to the limited heat exchange with the sidewalls. Subsequently, as solidification progresses, intensified heat transfer from the sidewall direction fosters denser isotherms and a gradual upward movement of the solid–liquid interface relative to the mold top, culminating in a straighter pattern.

On the right side of Figure 5a,b, the characteristics of melt flow depict the formation of primary and secondary clockwise vortices at the initial stage. Under the influence of the weak vortex, the Ag element enriched near the sidewall is continuously transported to the central region, resulting in enrichment of the Ag element there. This process occurs when the height of the directionally solidified copper ingot is less than 135 mm (Stage 1 in Figure 4a). As the solidification process advances, the effect of heat transfer through the sidewall intensifies, and the solid–liquid interface moves upward along the height direction relative to the mold top. This ultimately leads to the disappearance of the weak vortex, as depicted in Figure 5c. Consequently, the Ag element near the sidewall is no longer transported to the central region. Moreover, the intensity of the primary vortex increases, potentially causing the Ag element to be entrained into the liquid phase above the solid–liquid interface, thereby reducing the Ag element content in the forefront of the solid–liquid interface. This process generally occurs when the solidification height of the copper ingot is within the range of 135 mm to 244 mm (Stage 2 in Figure 4a).

As the solidification process continues, the magnitude of the upward movement of the solid–liquid interface becomes less pronounced, as shown in Figure 5d–f. The impurity element Ag may experience a slight influence from the primary vortex and once again exhibit a tendency to gradually accumulate toward the axial centerline of the ingot. This phenomenon occurs when the solidification height of the copper ingot is within the range of 244 mm to 373 mm (Stage 3 in Figure 4a). When the solidification height of the copper ingot exceeds 373 mm, there is insufficient melt replenishment from the crucible above. Consequently, during the late stage of solidification, the Ag element content sharply increases as the residual melt completely solidifies (Stage 4 in Figure 4a).

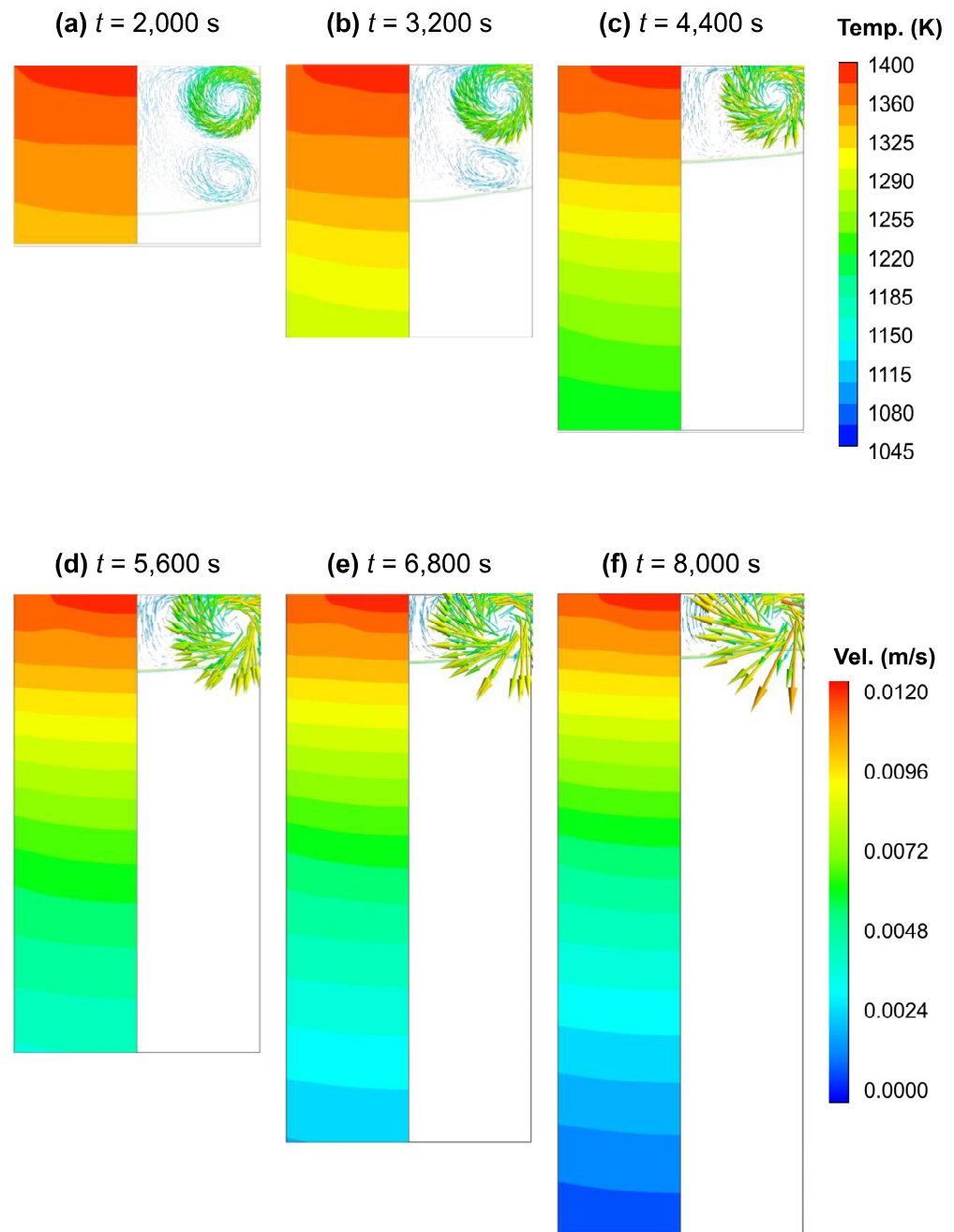


Figure 5. Simulated temporal evolution of the temperature field, flow field, and solid–liquid interface during the solidification process. Melt temperature of 1400 K and a pulling rate of 50 $\mu\text{m/s}$.

3.2. Impact of Process Parameters on Spatial Distribution during the Semi-Continuous Directional Solidification Process

This section elucidates the influence of the pulling rate and melt temperature on the spatial distribution of impurities within copper ingots during the semi-continuous directional solidification process. Numerical simulations were conducted to analyze the Ag content along the axial centerline under six varying process conditions, as depicted in Figure 6. The findings indicate that increasing the pulling rate while maintaining a constant melt temperature significantly enhances the segregation degree of the impurity element Ag. In contrast, keeping the pulling rate constant while altering the melt temperature yields diverse effects on the axial Ag content. For instance, at a pulling rate of 25 $\mu\text{m/s}$ and a melt temperature of 1400 K, the Ag content steadily increases during solidification. However, at a higher melt temperature of 1420 K, an initial rise followed by a slight decrease in

Ag content along the axial centerline is observed. Similarly, at a pulling rate of $50 \mu\text{m/s}$, the Ag content initially increases and then slightly decreases along the axial centerline, regardless of the melt temperature. Notably, the location of the maximum Ag content differs depending on the melt temperature, occurring around the solidification height of 135 mm for a melt temperature of 1400 K and approximately at the solidification height of 247 mm for a melt temperature of 1420 K. Furthermore, increasing the pulling rate to $100 \mu\text{m/s}$ results in a continuous increase in Ag content along the ingot's axial centerline under both melt temperatures.

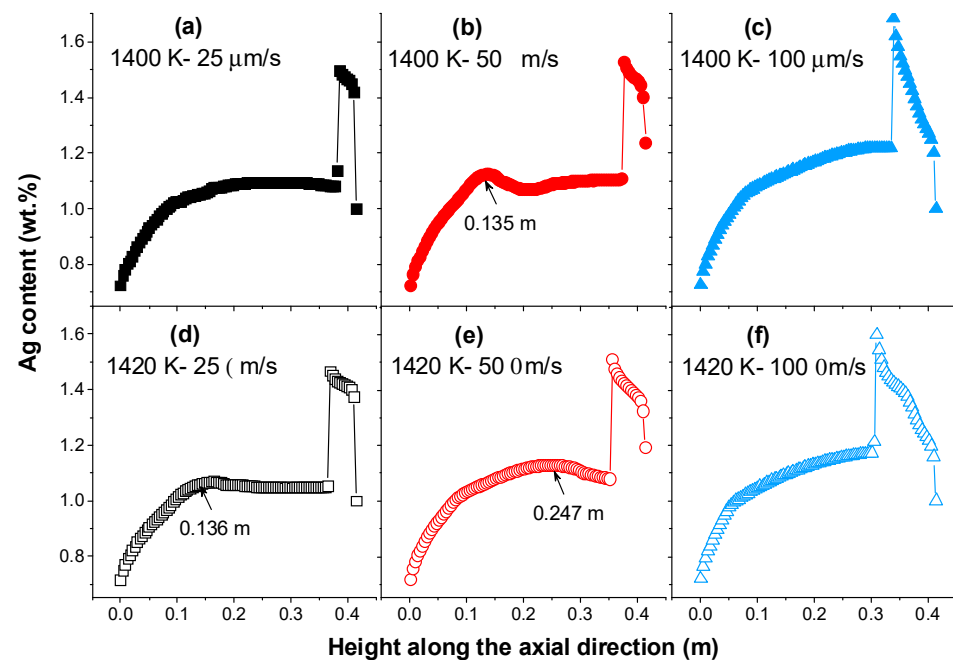


Figure 6. Simulated axial distribution of the impurity element Ag along the central axis of the copper ingot under various melt temperature and pulling rate conditions.

Figure 7 illustrates the radial distribution curves of the impurity element Ag content at different heights of the copper ingot under various process conditions. It is observed that the Ag content exhibits a central enrichment feature along the ingot's radius, presenting an "A-type" characteristic. Increasing the pulling rate intensifies the degree of Ag element enrichment from the sidewall toward the center of the copper ingot. However, alterations in melt temperature do not produce a consistent pattern in the radial distribution of the Ag content. Specifically, at a pulling rate of $25 \mu\text{m/s}$, the radial distribution of Ag content rapidly increases with increasing ingot solidification height and then stabilizes (Figure 7a,d). Similarly, at a pulling rate of $50 \mu\text{m/s}$, the distribution trend mirrors that of a pulling rate of $25 \mu\text{m/s}$ (Figure 7b,e). However, the radial distribution at a pulling rate of $100 \mu\text{m/s}$ continuously increases with solidification height, differing from the trends observed at lower pulling rates (Figure 7c,f). The impact of pulling rate on the distribution of the impurity element Ag appears more significant than the melt temperature adjustments.

Further insights are gained through numerical simulations analyzing the Ag distribution, temperature field, and flow field under various conditions at a copper ingot solidification height of 250 mm. Figure 8 illustrates that increasing the pulling rate and melt temperature results in a noticeable downward shift in the solid–liquid interface relative to the mold top. The changes in the position and shape of the solid–liquid interface are consistent with the results reported in the literature [28].

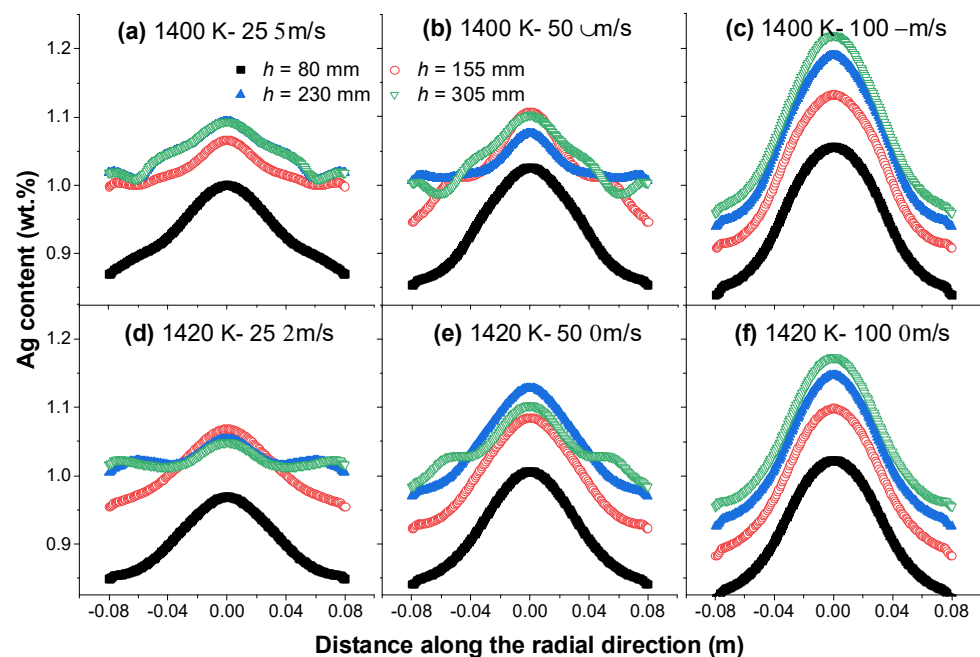


Figure 7. Simulated radial distribution of the impurity element Ag at different ingot heights under various melt temperature and pulling rate conditions.

Figure 9 reveals that increasing the pulling rate enhances the melt velocity at the mold's inlet, causing sparse isotherms (lower temperature gradient), while the melt flow intensity diminishes. Conversely, increasing the melt temperature strengthens the melt flow. As shown in Figure 9a–c, the maximum melt velocities along the axial centerline are 0.0108 m/s, 0.0095 m/s, and 0.0085 m/s, respectively, while in Figure 9d–f, the maximum velocities are 0.0112 m/s, 0.0103 m/s, and 0.0093 m/s, respectively. The continuous enhancement in the presence of the impurity element Ag along the ingot's axial centerline with increasing pulling rate and/or melt temperature is inferred to be the combined effect of the thermal gradient and melt flow, leading to the varying downward shift in the solid–liquid interface relative to the mold top. Consequently, this results not only in the formation of the primary vortex flow above the melt but also possibly in an additional weak vortex. Under the influence of this secondary weak vortex, impurities are continuously transported toward the central region. This phenomenon differs from the single-vortex flow of the melt during direct-chill casting, where the pulling rate is relatively high at approximately 1000 $\mu\text{m/s}$. While there were some slight changes in the shape of the mushy zone during the downward pulling process, no secondary vortex appeared [32,33].

To characterize the impurity separation efficiency of the semi-continuous directional solidification method, the three-dimensional integration of Ag content along the height direction of the copper ingot was performed, yielding the distribution curve of the average Ag content depicted in Figure 10. These curves exhibit a similar pattern under different process conditions, characterized by a gradual increase followed by stabilization, with a rapid increase in Ag content at the late stage of solidification. However, it is crucial to note that at a melt temperature of 1400 K, the critical solidification heights for the rapid increase corresponding to pulling rates of 25 $\mu\text{m/s}$, 50 $\mu\text{m/s}$, and 100 $\mu\text{m/s}$ are 387 mm, 376 mm, and 350 mm, respectively, while at a melt temperature of 1420 K, the critical solidification heights corresponding to the three pulling rates are 373 mm, 360 mm, and 322 mm, respectively. Clearly, the critical solidification heights decrease significantly with increasing pulling rate and melt temperature, indicating that lower pulling rates and melt temperatures are advantageous for more effective impurity separation within the ingot.

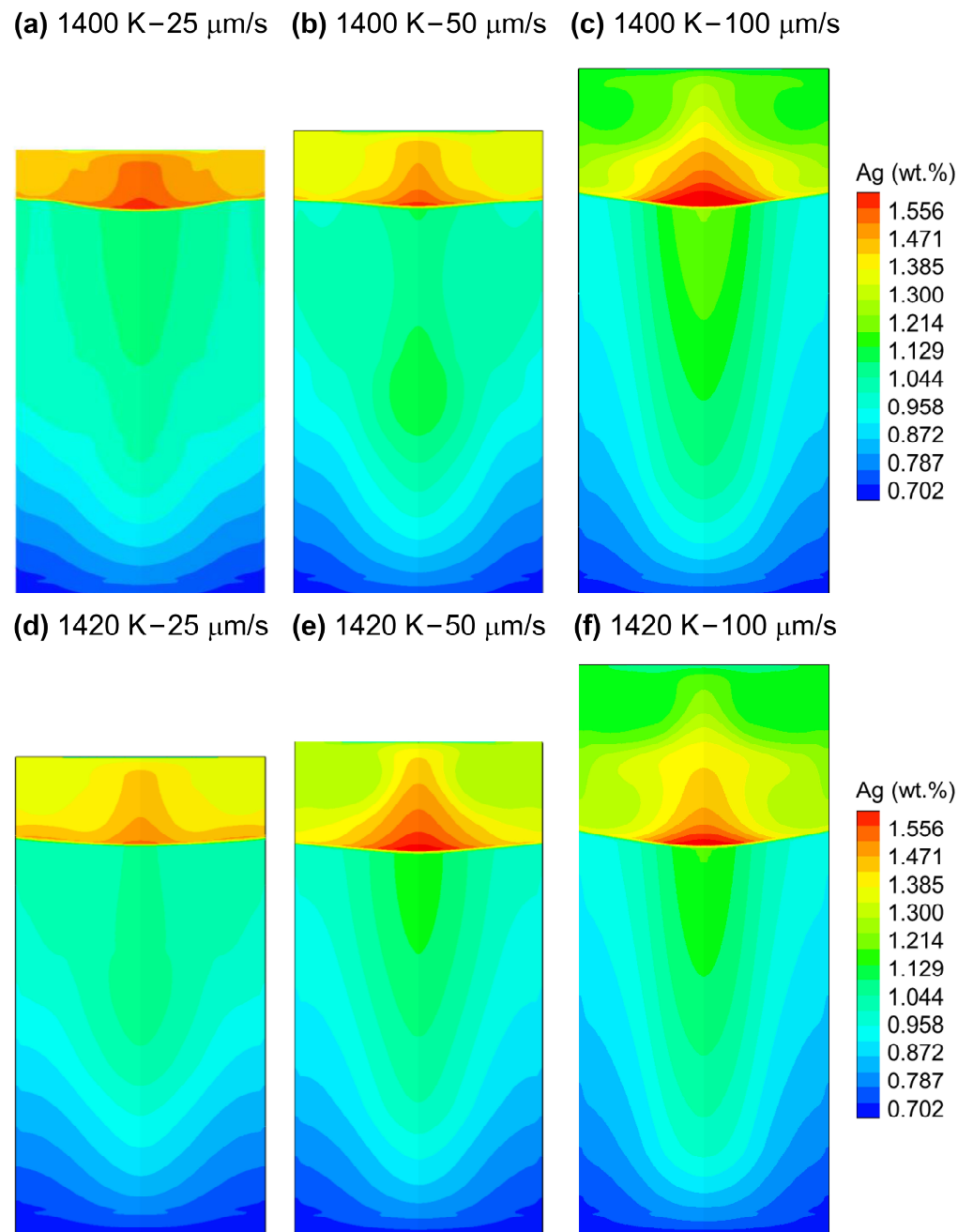


Figure 8. Simulated spatial distribution of the impurity element Ag within the copper ingot at a solidification height of 250 mm under six distinct melt temperature and pulling rate conditions.

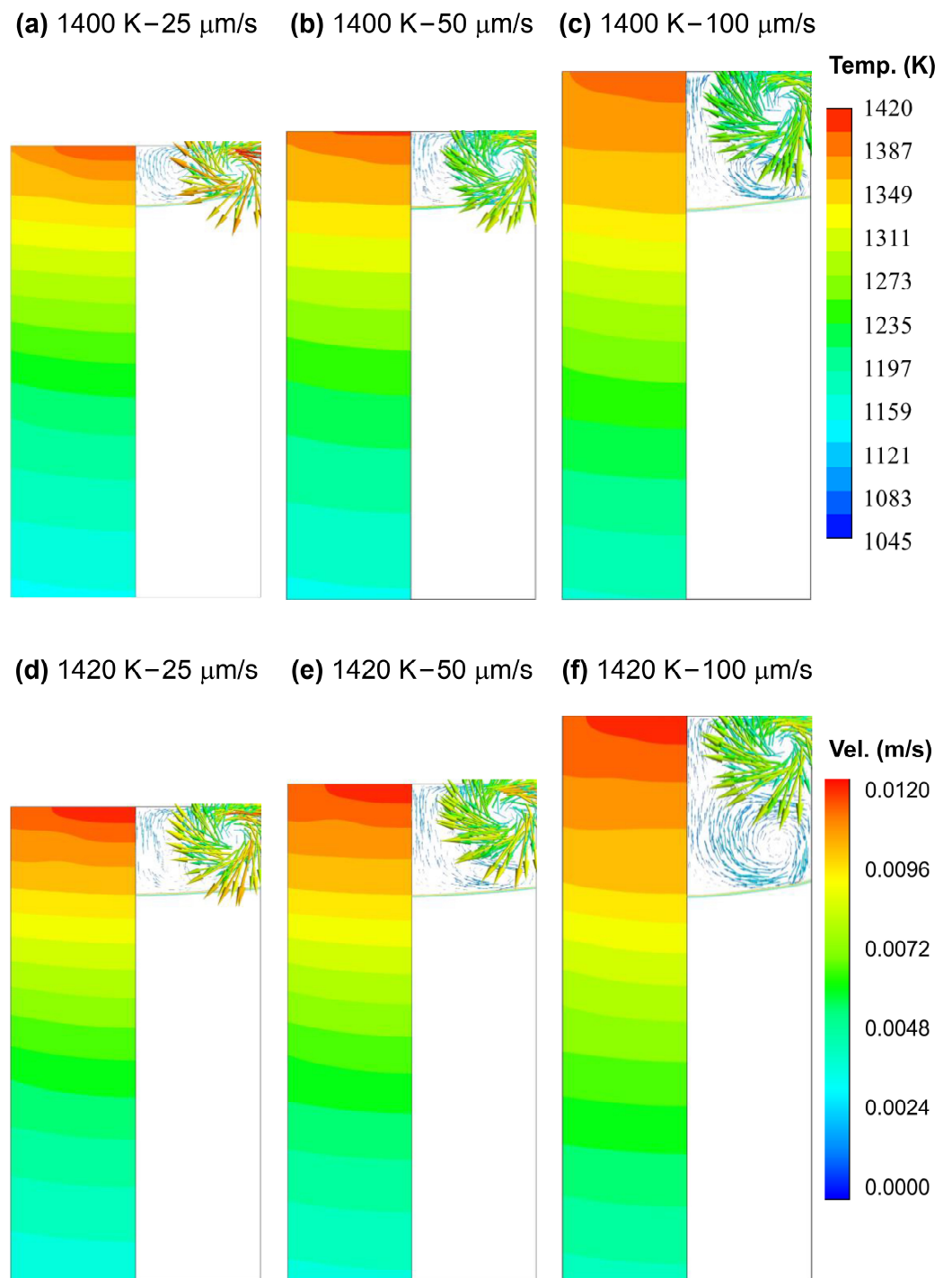


Figure 9. Simulated characteristics of the temperature field, flow field, and solid–liquid interface at a solidification height of 250 mm under various melt temperature and pulling rate conditions.

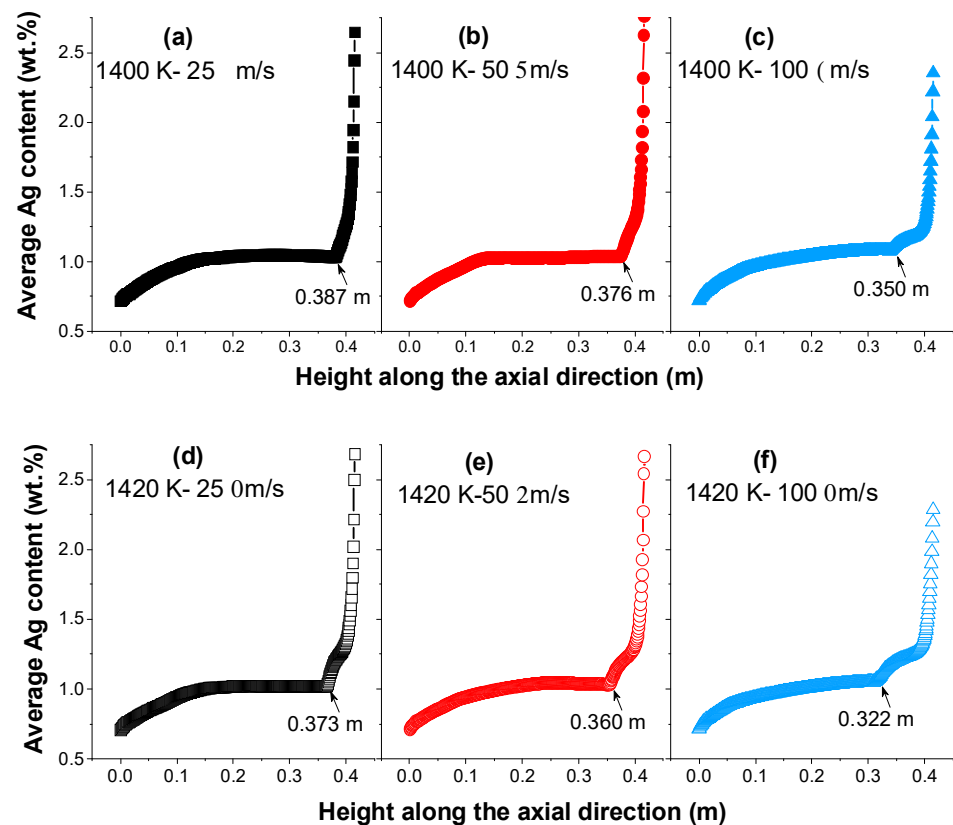


Figure 10. Simulated distribution of the average content of the impurity element Ag along the ingot height under various melt temperature and pulling rate conditions.

3.3. Experimental Validation of High-Purity Copper Purification via the Semi-Continuous Directional Solidification Process

This section experimentally validates the efficacy of purifying high-purity copper from 4N-grade recycled copper raw material through a semi-continuous directional solidification process. Given the complexity of large-scale production experiments and the sensitivity of industrial data, a feasibility study was conducted in a small-scale semi-continuous directional solidification furnace in the laboratory to mimic real-world production conditions as closely as possible. Based on the understanding of process parameters' influence on impurity migration, a relatively low pulling rate of 25 $\mu\text{m/s}$ was selected. The produced high-purity copper ingot had dimensions of 64 mm for its diameter and approximately 155 mm for its total length. Figure 11 illustrates the melting of approximately 4.5 kg of recycled copper raw material followed by downward pulling and shows the appearance of the obtained high-purity copper ingot. Sampling for impurity detection was performed at the 1/4 and 3/4 positions along the axial height direction, corresponding to Sample-1 and Sample-2, respectively. The purification was assessed through quantitative impurity analysis using glow discharge mass spectrometry (GDMS), and the GDMS test sample had dimensions of 20 mm \times 20 mm \times 6 mm. The results of the impurity detection analysis are summarized in Table 2.

The purity of the recycled copper raw material, determined from melt sampling, was 99.9957 wt.%. After the semi-continuous directional solidification experiment, the content of six impurities (As, Bi, Mn, Pb, Sb, and Sn) at both sampling positions was below the GDMS instrument's detection limit of 0.005 ppm. Furthermore, a significant decrease was observed in the content of Ag, Al, Ca, Fe, Zn, Cr, Co, and Cd. Notably, the Ca content decreased from 22.090 ppm to 0.045 ppm and 0.068 ppm. However, separating Ni and Si elements presented a relatively greater challenge, suggesting that their partition coefficients may be close to 1 or that they may have formed compounds with copper or interacted with other impurity elements in the melt under the given process conditions. The ingot's

purity at the 1/4 and 3/4 positions along the axial height direction reached a 5N grade, measuring 99.9994 wt.% and 99.9993 wt.%, respectively. Although the experimental work in this study did not strictly replicate the dimensions or thermal boundary conditions of large-scale high-purity copper production, when combined with the spatial distribution characteristics of impurity elements within the ingot, it could be inferred that the overall 5N production yield would be 75% or higher. This yield is comparable to vertical zone refining [34] but significantly higher than horizontal zone refining, which typically ranges between 40% and 60% [16–18,35].

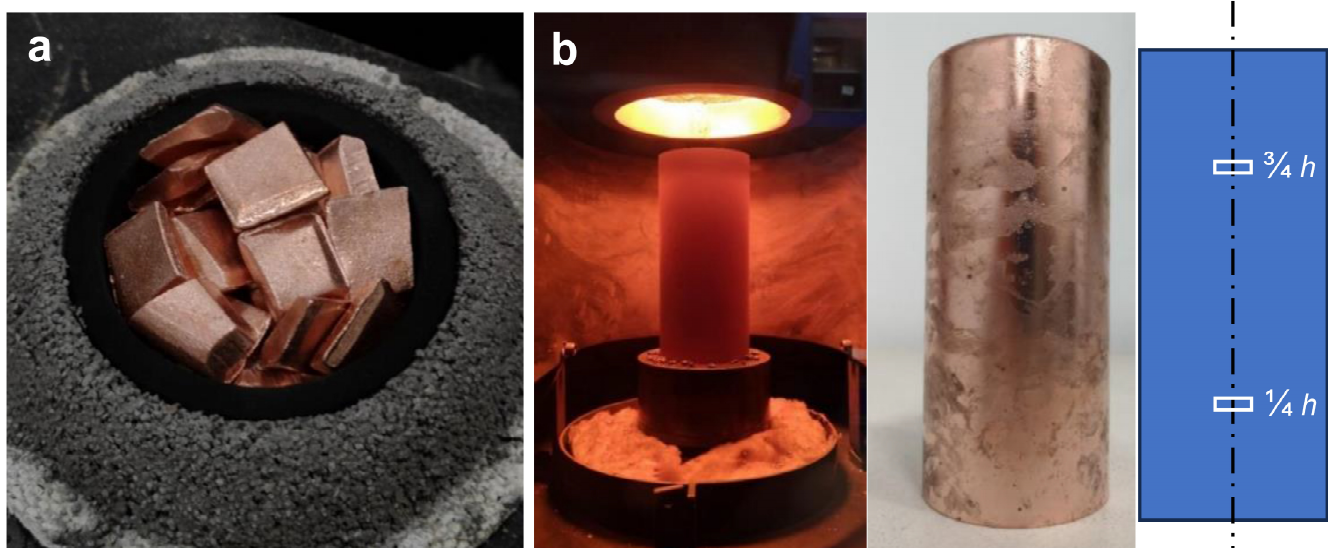


Figure 11. (a) Recycled copper raw material used. (b) High-purity copper ingot obtained by the semi-continuous directional solidification process. Sampling positions along the ingot axial direction for GDMS analysis are indicated.

Table 2. GDMS analysis results showing impurity concentrations (in ppm) in the recycled copper raw material and the high-purity copper ingot purified via the semi-continuous directional solidification process at different axial heights.

Impurity	Raw Material	Sample-1	Sample-2	Impurity	Raw Material	Sample-1	Sample-2
Ag	0.37	0.02	0.031	Fe	4.64	0.18	0.18
Al	1.15	0.033	0.032	Mn	0.09	—	—
As	0.66	—	—	Ni	4.76	4.03	4.24
Bi	1.04	—	—	Pb	0.04	—	—
Ca	22.09	0.045	0.068	Sb	0.28	—	—
Cd	0.04	0.018	0.01	Sn	0.29	—	—
Co	0.05	0.017	0.019	Zn	2.55	0.016	0.008
Cr	1.45	0.42	0.44	Si	3.20	1.62	2.02
Total content	42.70	6.40	7.05	"—" indicates content below the GDMS detection limit.			
Purity (wt.%)	99.9957	99.9994	99.9993				

These experimental results strongly confirm the effectiveness of the semi-continuous directional solidification method for practical high-purity copper impurity separation applications. To further enhance purity levels in subsequent large-scale production, it is suggested that the top 25% portion of the ingot be removed, like in the Czochralski method [36,37], followed by one or two additional directional solidification cycles. Meanwhile, to balance production efficiency and purity, a relatively higher pulling rate could be considered during the initial stage, while a relatively lower rate could be employed during the late stage, with the aim of delaying the rapid impurity ascent and achieving

a higher production yield. Alternatively, for challenging-to-remove Ni and Si elements, high-temperature vacuum distillation of the copper melt for an appropriate duration could be considered before initiating the directional solidification purification process.

4. Conclusions

The present study employed numerical simulations to analyze the multi-physics interactions during the semi-continuous directional solidification process, using a Cu-1 wt.% Ag model alloy. The objective was to investigate the impact of two crucial process parameters—pulling rate and melt temperature—on the distribution patterns of the impurity element Ag. Several significant findings emerged:

1. Increasing the pulling rate and melt temperature causes a downward shift in the solid–liquid interface relative to the mold top. This shift, influenced by thermal gradients and flow dynamics, induces the formation of a secondary weak vortex in the melt near the sidewall region in addition to the primary clockwise vortex flow. This phenomenon facilitates the migration of the impurity element Ag toward the central axis of the ingot, leading to amplified radial fluctuations in the Ag content.
2. A consistent trend is observed along the ingot's height regarding the purification efficiency of high-purity copper through semi-continuous directional solidification. The average Ag content demonstrates a gradual increase, followed by stabilization and an eventual rapid ascent during the late stage of solidification. With an increased pulling rate and melt temperature, the stage of rapid ascent occurs earlier. This suggests that lower pulling rates and melt temperatures are advantageous for purifying high-purity copper.
3. Experimental validation using 4N-grade recycled copper raw material in a small-scale semi-continuous directional solidification apparatus at a pulling rate of 25 $\mu\text{m/s}$ demonstrated the feasibility of this method for high-purity copper production. Copper samples extracted at 1/4 and 3/4 ingot heights achieved a 5N purity level of 99.9994 wt.% and 99.9993 wt.%, respectively.

Author Contributions: Conceptualization, H.Z.; methodology, H.Z.; validation, Y.W. and L.Z.; formal analysis, Y.W., L.Z., Y.Z. and H.Z.; investigation, Y.W.; resources, L.Z.; data curation, Y.W. and L.Z.; writing—original draft preparation, Y.W.; writing—review and editing, Y.Z. and H.Z.; visualization, Y.W.; supervision, H.Z.; project administration, H.Z.; funding acquisition, H.Z. All authors have read and agreed to the published version of the manuscript.

Funding: This work was supported by the National Natural Science Foundation of China (52074180) and the Science and Technology Major Project of Yunnan Province (202302AB080020).

Data Availability Statement: The data presented in this study are available within the article.

Conflicts of Interest: The authors declare no conflicts of interest.

References

1. Kato, M. The production of ultrahigh-purity copper for advanced applications. *JOM* **1995**, *47*, 44–46. [[CrossRef](#)]
2. Zhang, H.; Wang, S.; Tian, Y.H.; Wen, J.Y.; Hang, C.J.; Zheng, Z.; Huang, Y.L.; Ding, S.; Wang, C.X. High-efficiency extraction synthesis for high-purity copper nanowires and their applications in flexible transparent electrodes. *Nano Mater. Sci.* **2020**, *2*, 164–171. [[CrossRef](#)]
3. Oishi, T.; Koyama, K.; Alam, S.; Tanaka, M.; Lee, J.C. Recovery of high purity copper cathode from printed circuit boards using ammoniacal sulfate or chloride solutions. *Hydrometallurgy* **2007**, *89*, 82–88. [[CrossRef](#)]
4. Li, Z.J.; Wang, W.; Jiang, L.J.; Chang, Z.D.; Ma, X.P.; Luo, X. Effects of acid pretreatment on purity of copper foil recovered by electrolytic refining from waste printed circuit board. *Waste Biomass Valorization* **2024**, *15*, 1403–1410. [[CrossRef](#)]
5. Randhawa, N.S.; Sau, D.C.; Kumar, M. Direct electrolytic refining of end-of-life industrial copper waste scraps for production of high purity copper powder. *Russ. J. Non-Ferrous Met.* **2016**, *57*, 367–373. [[CrossRef](#)]
6. Fan, H.Q.; Zhu, X.; Zheng, H.X.; Lu, P.; Wu, M.Z.; Peng, J.B.; Zhang, H.S.; Qian, Q. Machine learning-based multi-objective parameter optimization for indium electrorefining. *Sep. Purif. Technol.* **2024**, *328*, 125092. [[CrossRef](#)]
7. Ding, L.F.; Cheng, J.; Wang, T.; Zhao, J.L.; Chen, C.Y.; Niu, Y.L. Continuous electrolytic refining process of cathode copper with non-dissolving anode. *Miner. Eng.* **2019**, *135*, 21–28. [[CrossRef](#)]

8. Wang, J.Q.; Chen, S.Y.; Zeng, X.F.; Huang, J.F.; Liang, Q.; Shu, J.C.; Chen, M.J.; Xiao, Z.X.; Zhao, H.B.; Sun, Z. Recovery of high purity copper from waste printed circuit boards of mobile phones by slurry electrolysis with ammonia-ammonium system. *Sep. Purif. Technol.* **2021**, *275*, 119180. [[CrossRef](#)]
9. Wang, D.; Wang, L.P.; Yu, H.S.; Tian, Y.; Yang, B.; Xu, B.Q.; Liang, D.; Ma, T.Z. Preparation of high-purity copper through vacuum distillation. *Vacuum* **2023**, *218*, 112566. [[CrossRef](#)]
10. Liu, W.; Ma, B.Z.; Zhou, Z.G.; Zuo, Y.C.; Wang, L.; Chen, Y.Q.; Wang, C.Y. Efficient separation of impurities in scrap copper by sulfurization-vacuum distillation. *Vacuum* **2022**, *202*, 111145. [[CrossRef](#)]
11. Guo, X.Y.; Zhou, Y.; Zha, G.Z.; Jiang, W.L.; Yang, B.; Ma, W.H. A novel method for extracting metal Ag and Cu from high value-added secondary resources by vacuum distillation. *Sep. Purif. Technol.* **2020**, *242*, 116787. [[CrossRef](#)]
12. Zhan, L.; Qiu, Z.L.; Xu, Z.M. Separating zinc from copper and zinc mixed particles using vacuum sublimation. *Sep. Purif. Technol.* **2009**, *68*, 397–402. [[CrossRef](#)]
13. Sun, J.L.; Zhang, J.; Wang, H.W.; Wang, T.M.; Cao, Z.Q.; Lu, Y.P.; Li, T.J. Purification of metallurgical grade silicon in an electron beam melting furnace. *Surf. Coat. Technol.* **2013**, *228*, S67–S71. [[CrossRef](#)]
14. Long, L.P.; Liu, W.S.; Ma, Y.Z.; Liu, Y.; Liu, S.H. Refining tungsten purification by electron beam melting based on the thermal equilibrium calculation and tungsten loss control. *High Temp. Mater. Process.* **2015**, *34*, 605–610. [[CrossRef](#)]
15. Vutova, K.; Donchev, V. Electron beam melting and refining of metals: Computational modeling and optimization. *Materials* **2013**, *6*, 4626–4640. [[CrossRef](#)] [[PubMed](#)]
16. Dosmukhamedov, N.K.; Zholdasbay, E.E.; Nurlan, G.B. Ultra-pure Cu obtaining using zone melting: Influence of liquid zone width on impurities' behavior. *Russ. J. Non-Ferrous Met.* **2017**, *43*, 15–20. [[CrossRef](#)]
17. Wan, H.L.; Kong, L.X.; Yang, B.; Xu, B.Q.; Duan, M.P.; Dai, Y.N. Zone melting under vacuum purification method for high-purity aluminum. *J. Mater. Res. Technol.* **2022**, *17*, 802–808. [[CrossRef](#)]
18. Zhang, X.X.; Friedrich, S.; Friedrich, B. Separation behavior of arsenic and lead from antimony during vacuum distillation and zone refining. *J. Mater. Res. Technol.* **2020**, *9*, 4386–4398. [[CrossRef](#)]
19. Zhu, Y.F.; Mimura, K.; Ishikawa, Y.; Isshiki, M. Effect of floating zone refining under reduced hydrogen pressure on copper Purification. *Mater. Trans.* **2002**, *43*, 2802–2807. [[CrossRef](#)]
20. Fu, Y.B.; Chen, J.; Liu, N.; Lu, Y.P.; Li, T.J.; Yin, G.M. Study of ultrahigh-purity copper billets refined by vacuum melting and directional solidification. *Rare Met.* **2011**, *30*, 304–309. [[CrossRef](#)]
21. Huang, F.; Chen, R.R.; Guo, J.J.; Ding, H.S.; Su, Y.Q. Removal of metal impurities in metallurgical grade silicon by cold crucible continuous melting and directional solidification. *Sep. Purif. Technol.* **2017**, *188*, 67–72. [[CrossRef](#)]
22. Kazup, Á.; Kárpáti, V.; Hegedüs, B.; Gácsi, Z.; Ferenczi, T. High purity primary aluminum casting by INDUTHERM CC3000 semi-continuous casting equipment. In Proceedings of the MultiScience—XXXIII, microCAD International Multidisciplinary Scientific Conference, Miskolc, Hungary, 23–24 May 2019.
23. Bennon, W.D.; Incropera, F.P. A continuum model for momentum, heat and species transport in binary solid-liquid phase change systems—I. Model formulation. *Int. J. Heat Mass Transfer* **1987**, *30*, 2161–2170. [[CrossRef](#)]
24. Bennon, W.D.; Incropera, F.P. A continuum model for momentum, heat and species transport in binary solid-liquid phase change systems—II. Application to solidification in a rectangular cavity. *Int. J. Heat Mass Transfer* **1987**, *30*, 2171–2187. [[CrossRef](#)]
25. Jeong, C.H.; Kang, K.; Park, U.J.; Lee, H.J.; Kim, H.S.; Park, J.Y.; Lee, S.H. Numerical investigation on the evolution of thin liquid layer and dynamic behavior of an electro-thermal drilling probe during close-contact heat transfer. *Appl. Sci.* **2021**, *11*, 3443. [[CrossRef](#)]
26. Song, H.B.; Wang, Y.H.; Peng, J.P.; Liu, C.C. Study on the uniformity of temperature distribution of transverse flux induction heating based on a new magnetic pole. *Energies* **2022**, *15*, 7450. [[CrossRef](#)]
27. Safa, Y.; Flueck, M.; Rappaz, J. Numerical simulation of thermal problems coupled with magnetohydrodynamic effects in aluminium cell. *Appl. Math. Modell.* **2009**, *33*, 1479–1492. [[CrossRef](#)]
28. Jia, Y.H.; Zhao, D.Z.; Li, C.Y.; Bao, L.; Le, Q.C.; Wang, H.; Wang, X. Study on solidification structure evolution of direct-chill casting high purity copper billet using cellular automaton-finite element method. *Metals* **2020**, *10*, 1052. [[CrossRef](#)]
29. Kawecki, A.M.; Knych, T.; Sieja-Smaga, E.; Mamala, A.; Kwaśniewski, P.; Kiesiewicz, G.; Smyrak, B.; Pacewicz, A. Fabrication, properties and microstructures of high strength and high conductivity copper-silver wires. *Arch. Metall. Mater.* **2012**, *57*, 1261–1270. [[CrossRef](#)]
30. Li, Y.; Wang, X.F.; Yin, S.; Xu, S.L. Influence of particle initial temperature on high velocity impact process in cold spraying. *Procedia Environ. Sci.* **2012**, *12*, 298–304. [[CrossRef](#)]
31. Huang, F.; Zhao, L.; Liu, L.; Hu, Z.L.; Chen, R.R.; Dong, Z.L. Separation and purification of Si from Sn-30Si alloy by electromagnetic semi-continuous directional solidification. *Mater. Sci. Semicond. Process.* **2019**, *99*, 54–61. [[CrossRef](#)]
32. Luo, H.J.; Jie, W.Q.; Gao, Z.M.; Zheng, Y.J. Effects of casting parameters on macrosegregation in 2024 alloy during direct-chill casting based on numerical simulation. *Rare Met. Mater. Eng.* **2018**, *48*, 2759–2767.
33. Chen, Q.P.; Li, H.X.; Shen, H.F. Transient modeling of grain structure and macrosegregation during direct chill casting of Al-Cu alloy. *Processes* **2019**, *7*, 333. [[CrossRef](#)]
34. Li, M.X.; Tian, Q.L.; Wu, M.Z.; Peng, J.B.; Zhang, J.T.; Chen, L.S.; Lu, X.W.; Xu, Z.S.; Zheng, H.X. Numerical simulation analysis on solute redistribution of In-1 wt% Sn alloy during multipass vertical zone refining process. *J. Cryst. Growth* **2021**, *565*, 126156. [[CrossRef](#)]

35. Prasad, D.; Munirathnam, N.; Rao, J.; Prakash, T. Effect of multi-pass, zone length and translation rate on impurity segregation during zone refining of tellurium. *Mater. Lett.* **2006**, *60*, 1875–1879. [[CrossRef](#)]
36. Abrosimov, N.; Czupalla, M.; Dropka, N.; Fischer, J.; Gybin, A.; Irmscher, K.; Janicskó-Csáthy, J.; Juda, U.; Kayser, S.; Miller, W.; et al. Technology development of high purity germanium crystals for radiation detectors. *J. Cryst. Growth* **2020**, *532*, 125396. [[CrossRef](#)]
37. Wang, G.J.; Mei, H.; Mei, D.M.; Guan, Y.T.; Yang, G. High purity germanium crystal growth at the University of South Dakota. *J. Phys. Conf. Ser.* **2015**, *606*, 012012. [[CrossRef](#)]

Disclaimer/Publisher’s Note: The statements, opinions and data contained in all publications are solely those of the individual author(s) and contributor(s) and not of MDPI and/or the editor(s). MDPI and/or the editor(s) disclaim responsibility for any injury to people or property resulting from any ideas, methods, instructions or products referred to in the content.